Measurement of the Rate Coefficient for the Recombination of He^+ with Electrons*

C. B. Collins, H. S. Hicks,† W. E. Wells,‡ and R. Burton§
University of Texas at Dallas, Texas 75230
(Received 6 July 1970; revised manuscript received 27 March 1972)

A computer-linked spectroscopic system with a high-sensitivity-resolution product has been used to measure the time-dependent net rate of production of neutral helium atoms resulting from the recombination of He^+ with electrons in a pulsed helium afterglow at neutral pressures of 1.86 and 44.6 Torr. The recombination-rate coefficient of He^+ as a function of afterglow time has been obtained by dividing these data by the product of the electron and atomic-ion density as determined from intensity measurements of radiation from bound levels in Saha equilibrium with the free electrons. Simultaneous time-resolved measurement of the electron density with a 35-GHz Fabry-Perot resonator has given the recombination-rate coefficient as a continuous function of electron densities without the need of *a priori* assumptions about that functional form. The electron temperature as a function of electron density in the recombining afterglow was determined from analyses of time-resolved measurements of the intensity distribution of radiation from the continuum states above the $n\,^3P \rightarrow 2\,^3S$ Rydberg series in atomic helium. For pressures below a nominal 2 Torr, the resulting parametrization of the recombination-rate coefficient for He^+ with electrons can be represented as $\alpha = 7.1\times10^{-20}(T/300)^{-4.3}[e]$ cm^3/sec, where T is the electron temperature and $[e]$ the electron density. At higher pressures the rate coefficient is found to decrease as a consequence of associative ionization of the excited states.

I. INTRODUCTION

The concept of collisionally stabilized recombination was originally developed[1-4] to explain the relatively large recombination rates which had been found for ion systems incapable of dissociative recombination.[5] Subsequent expectations were that both ions of helium, He^+ and He_2^+, would be found to recombine by this process. However, it was only under the limiting conditions of low neutral gas pressure and high electron density that the actual experimental measurements[6-9] of the rate of recombination of electrons with helium ions were brought into reasonable agreement with that theory. As reviewed in a previous article,[10] at higher pressure the variance between measurements had been considerable with some of them indicating dependence on both electron density and pressure and others showing dependence on only one or neither parameter.

The recent renewal of interest[10-12] in the measurement of the rate of recombination of electrons with helium ions has had as a specific focus the determination of the dependence of the rate coefficient upon experimental parameters. These measurements have benefited from the technological advances in photon counting, data acquisition, microwave interferometry, and in some cases[10,11] have converged upon characteristic electron removal rates. More important, however, is that these recent measurements have indicated the factors which most probably account for the poor agreement with the theory of collisionally stabilized recombination. In particular, it appears that most prior measurements have been performed upon a mixture of ion types including He^+, He_2^+, and He_3^+, and that the relative abundance of each was a continuously changing function of experimental parameters. In addition, in those measurements the electron temperature may have been varying with the changing parameters as a consequence of the return of energy to the electron gas during the course of the stabilizing collisions. Since the theory is generally isothermal and indicates a strong dependence on electron temperature, agreement could not be determined without independent knowledge of the temperature. A further complication has been indicated by Johnson and Gerardo,[12] who report that a significant fraction of recombination events in helium may be offset in their measurement scheme by persistent sources of ionization which must also be functions of the varied experimental parameters. In view of these complications, it appears that a critical test of theory is contingent upon the satisfaction of at least the following three conditions:

(i) The recombination of a single ion type needs to be examined as a function of the experimentally varied parameters.

(ii) The electron temperature should be determined as a function of the varied parameters.

(iii) The analysis techniques need to be insensitive to sources of ionization.

Recently, the authors have described[10] a technique for directly measuring the rate coefficients for the recombination of ions and electrons in laboratory plasmas without the need of *a priori* assumptions about the functional dependence of the

coefficient on experimental parameters. The method will be shown in the following material to be unaffected by ambient sources of ionization. The availability of this technique has made possible measurement of the recombination of the minority, as well as the dominant, ions at localized positions in an afterglow.

This paper reports the results of the simultaneous measurement of electron temperature and rate coefficient for the collisionally stabilized recombination of He^+ in a pulsed helium afterglow at neutral gas pressures of 1.86 and 44.6 Torr. Electron densities spanned portions of three orders of magnitude, 10^9 to 10^{12} cm^{-3}. Excellent agreement was found with earlier[7] high-temperature measurements and good agreement was found with the early theory[1] of collisional-radiative recombination which considered only radiation and stabilizing collisions with electrons. No evidence was found of the predicted[2-4] importance of stabilizing collisions with neutral atoms.

II. METHODS

A. Determination of Recombination-Rate Coefficient

The process of collisionally stabilized recombination is a composite of a considerable number of constituent processes. However, for values of parameters characteristic of most laboratory plasmas it can be conveniently considered to occur in two steps, electron capture and subsequent stabilization. The initial captures, together with their necessary inverse processes, can proceed according to the several mechanisms discussed in the previously cited literature. The net result is the establishment of a quasiequilibrium distribution of population among the bound states whose ionization potential is less than a few KT. The population of each such state can be considered to be in dynamic equilibrium with each other such state, as well as the collection of free states, ensuring that the population can be described by the modified Saha equation:

$$[X^*(q)] = [X^+][e]\frac{g(q)}{g^+ g_e}\left(\frac{2\pi m K T_e}{h^2}\right)^{-3/2} e^{U_q/KT}, \quad (1)$$

where $[X^+]$, $[X^*(q)]$, and $[e]$ are concentrations of X^+, the qth excited state of X, and the free electrons, respectively; g^+, $g(q)$, and g_e are the corresponding statistical weights; U_q is the ionization potential for $X^*(q)$; T_e and T are, respectively, the electron temperature and the distribution temperature, defined elsewhere,[13] for which

$$T_g \leq T \leq T_e , \quad (2)$$

with T_g denoting the heavy-particle temperature. Other symbols have conventional meanings. The total population within such states is necessarily small compared to the ion density in most laboratory afterglows and therefore does not represent a significant portion of the loss of ionization due to recombination. Under these conditions, the rate-limiting processes in the recombination sequence are the stabilization steps. Within the framework of accepted theories, net stabilization can occur by successive collisional or radiative processes which tend to move population to states of greater ionization potential. When an element of population has been moved to a level of sufficiently high ionization potential, the rates for the inverse excitation processes are negligible and the stabilization is complete. Consequently, the measurement of the net rate of production of stabilized neutrals is equivalent to the measurement of the rate of recombination. Equation (3) illustrates this point and serves to define the equivalent two-body recombination-rate coefficient α. When defined in this way, α is considered to be a function of electron density as well as other experimentally varying parameters:

$$\alpha[He^+][e] \equiv -\frac{d}{dt}[He^+]\Big|_R = \frac{d}{dt}[He(2)]\Big|_R + \frac{d}{dt}[He(1)]\Big|_R . \quad (3)$$

In this expression, $[He(p)]$ represents the concentration of He in a state with a principal quantum number p, and the subscripted R indicates that only the net rate of production or loss due to the recombination processes are to be considered. Terms for higher quantum levels need not be considered as the populations of these levels rapidly (10^{-6} sec) relax to quasiequilibrium values for which the time derivative is much less than the corresponding value for the ground and metastable levels.[1] Substituting into (3) for the net rates of production of the ground, metastable, and other $p = 2$ levels from recombination sources gives the following:

$$\alpha[He^+][e] = \sum_{i=1}^{2}\sum_{j=3}^{\infty} I(i, j) + \sum_{i=1}^{2}\sum_{j=3}^{\infty}\{K_e(i, j)[e] + K_N(i, j)[He]\}[He(j)], \quad (4)$$

where $I(i, j)$ represents the absolute intensity of all radiation from levels with principal quantum number j to levels with quantum number i, and $K_e(i, j)$ and $K_N(i, j)$ are the rate coefficients for the processes

$$He(j) + e \rightarrow He(i) + e, \qquad j > i \quad (5)$$

and

$$He(j) + He \rightarrow He(i) + He, \quad j > i \quad (6)$$

respectively. Theory indicates that the collision

terms of the second line of Eq. (4) can be neglected in comparison with the radiation terms. For example, the rate calculated[14] for the superelastic deexcitation by electron collisions of the $q=3$ levels of He is less than 5×10^{-9} cm^3/sec, which for most laboratory afterglows of moderate electron density ($<10^{12}$ cm^{-3}) means that neglect of this term would result in an error less than 0.2 or 0.3% of $I(2, 3)$. Similar neglect of the sum of intensity from transition directly to the ground state is warranted because of the strong imprisonment[15] of this radiation expected in systems of approximately liter volumes at Torr pressures.

The most significant error results from the truncation required by practical consideration of the infinite sum of intensities. Letting $I_K(2, j)$ represent the Kth member of the six spectral series connecting the jth to the second level, it can be shown by bounding the upper part of the sum with the spectral density emitted from the continuum associated with the particular Rydberg series considered, that

$$\sum_{j=3}^{\infty} I_K(2, j) = \sum_{j=3}^{6} I_K(2, j) + \epsilon\left(\sum_{j=7}^{Q} I_K(2, 7) + \frac{(KT)Q^3}{2\mathfrak{R}} I_K(2, Q)\right), \quad (7)$$

where $|\epsilon|<1$, $\mathfrak{R}$ is the Rydberg constant, and Q is an integer sufficiently large that Eq. (1) is satisfied. In practice, over the range of parameters covered by these experiments each term in the large parentheses represented about 5% of the sum of intensities truncated at six, the level arbitrarily chosen to limit the volume of data required. Substituting the leading term of (7) into (4) and rearranging terms gives the approximation to the recombination-rate coefficient which should be accurate to 10%,

$$\alpha = ([\mathrm{He}^+][e])^{-1} \sum_{K=1}^{6}\sum_{j=3}^{6} I_K(2, j). \quad (8)$$

Since

$$[\mathrm{He}_n(Q)] = I_n(2, Q)/A_n(2, Q), \quad (9)$$

where $A_n(2, Q)$ is the transition probability relating the intensity $I_n(2, Q)$ to the population $[\mathrm{He}_n(Q)]$ of the appropriate upper state, expressions (1), (8), and (9) can be combined to give the following expression for the recombination-rate coefficient in terms of experimentally measurable variables:

$$\alpha = \frac{g_n(Q)}{g^+ g_e}\left(\frac{2\pi mKT_e}{h^2}\right)^{-3/2} e^{U_q/kT}[I_n(2, Q]^{-1} A_n(2, Q) \times \sum_{K=1}^{6}\sum_{j=3}^{6} I_K(2, j). \quad (10)$$

B. Determination of Electron Temperature

As can be seen from Eq. (10), two temperatures need to be determined, the distribution temperature T and the electron temperature T_e. In principle, the first could be determined from Eq. (1) and measurement of a sequence of He*(q). Although this procedure is quite satisfactory for high-temperature afterglows,[7] attempts[9] to use it for nearly thermalized afterglows have met with considerable practical difficulties. In particular, since Eq. (1) is only valid within a few KT of the ionization limit, at low temperatures this requires the precise measurement of discrete spectral lines quite close to the recombination continuum. In fact, the transition from discrete lines to continuum is gradual, making the determination of the width of a single line very uncertain.

A more usable expression is obtained by smoothing Eq. (1), writing for $X(q)$, $\mathrm{He}(U_q)$, with the independent variable being ionization energy rather than principal quantum number,

$$\frac{d[\mathrm{He}(U)]}{dU} \equiv \frac{[\mathrm{He}(U_q)]}{\Delta U_q}, \quad (11)$$

where

$$\Delta U_q = U_q - U_{q-1}. \quad (12)$$

Recognizing that the transition probability is approximately

$$A_n(2, q) \propto q^{-3}, \quad (13)$$

then for large q,

$$A_n(2, q) \cong C\,\Delta U_q, \quad (14)$$

where C is an appropriate constant for scale. For a spectrometer with slits set so that the bandwidth ΔU_s, in terms of the ionization energy of the upper state radiating the transitions, is

$$\Delta U_s \ll KT, \quad (15)$$

the measured intensity $I_n(2, U)$ is given by

$$I_n(2, U) = G\int_{U}^{U+\Delta U_s} A_n(2, q(U'))\frac{d[\mathrm{He}(U')]}{dU'}\,dU', \quad (16)$$

G being the collected geometric factors. After substitution of (11), (14), and (1), the expression becomes

$$I_n(2, U)/\Delta U_s \cong C'\,e^{U/KT}, \quad (17)$$

where now C' represents the collected factors not dependent upon U and hence independent of detected wavelength for any particular set of afterglow parameters.

Expression (17) allows the use of both discrete lines and continuum since ΔU_s can be a function of U. In practice, the procedure is used of measuring values of $I_n(2, U_q)$ where it is possible to identify a $\Delta U_s = \Delta U_q$, and using uniformly spaced measurement of $I_n(2, U)$ otherwise. The distribution temperature then appears as the inverse slope of the curve of the logarithm on the left-hand side of

(17) plotted as a function of ionization energy corresponding to the wavelength and transition measured. Extending the measurements to the continuum radiation emitted during the process

$$He^+ + e \rightarrow He(2) + I(2,\ U_2 + E)\,, \tag{18}$$

where E the energy of the free electron e, gives the possibility of obtaining the free-electron temperature T_e in a similar manner from the part of the curve corresponding to negative ionization energies. In practice, since the transition from discrete lines to continuum is smooth, the application of Eq. (17) to intensity measurements spanning a range of wavelengths on both sides of the series limit suffices to determine both T and T_e.

A second and more convenient technique consists of comparing the total energy emitted in the states described by Eq. (1) and the energy emitted from the population of a single state. As can be seen from (17), the former will contain an extra multiplicative KT when the integration from some U_q to infinity is performed. Consequently, the expression

$$[I_n(2,\ q)]^{-1} \int_{U_q}^{\infty} I_n(2,\ U)\,dU \cong KTq^3/2\mathcal{R} \tag{19}$$

can be used to continuously monitor T as a function of time-varying experimental parameters, provided q is large enough that U_q satisfies Eq. (17). However, since it is possible to arrange $\Delta U_q < \Delta U_s \ll KT$, the first method, though less convenient, provides better sensitivity and hence better signal-to-noise ratios. The greater utility of the latter method is hence restricted to values of experimental parameters for which sufficient intensities are available.

C. Determination of Electron Density

Several methods are available for determining electron density, and the choice of a particular method is best dictated by the geometry of the plasma. The afterglow examined in these experiments occupies a large physical volume. As discussed in a related article,[16] in such systems, use of a microwave Fabry-Perot resonator provides a considerable advantage in sensitivity and spatial resolution over other devices such as free-space interferometers.

The basic data obtained with a Fabry-Perot resonator are a continuous record of the change in resonant frequency of the structure caused by the contained plasma. From this can be inferred the changing index of refraction of the afterglow and hence the electron density. Although the general analysis of such data is relatively straightforward in principle, a brief outline is presented for convenience. The principal complication is caused by the inclusion of quartz windows and other material in addition to the afterglow in the resonant structure.

In the zeroth approximation in which material boundaries are coincident with the standing wavefronts, the resonance condition can be written in terms of the contribution from each type of material i as

$$\sum_i n_i l_i = mC/2\nu_0\,, \tag{20}$$

where n_i and l_i are the index of refraction and thickness of the ith material in the cavity, C the velocity of light, ν_0 the frequency of the microwaves, and m an integer specifying the mode. If a change Δn_a occurs in the index of refraction in the afterglow region a, and the frequency is adjusted to restore resonance with the same m, then

$$\sum_i n_i l_i + \Delta n_a l_a = mC/2\nu_1\ . \tag{21}$$

Taking the differences of (21) and (20) and substituting the expressions[17] for the index of refraction in terms of electron density gives

$$[e] \cong 1.240 \times 10^{-8} (mC/l_a)\Delta\nu\,, \tag{22}$$

where l_a is in cm and $\Delta\nu$ is the frequency shift in Hz.

III. MEASUREMENT TECHNIQUES

A. Line Intensities

The quartz afterglow cell, gas-handling system, operational cycle, general instrumentation, and computer-linked data acquisition system have been discussed in earlier descriptions[9,18] of the pulsed afterglow system and were employed with few changes[10] in this experiment. An unfortunate consequence of the peculiar complexity of the gas-handling system made it quite difficult to change the experimental pressure. As a result, only two pressures were used for these measurements, 1.86 and 44.6 Torr. However, the same complexity also made system integrity quite high and in both cases was sufficient to ensure a variance of less than 15% in the time-resolved absolute intensity of various spectral features when remeasured after each few months of operation.

At the higher pressure, the experimental cell required 5-kV pulses of not greater than 10-μsec duration for dependable operation. Under these conditions, the discharge was observed to uniformly fill the region between electrodes. No arcs or constrictions occurred and the discharge appeared quite similar to the beam-excited discharges discussed by Persson,[19] for much lower pressures. At the 1.86-Torr pressure, 2-kV pulses of nominal 350-μsec duration were used. Improvements to the system introduced during the course of measurement at that pressure allowed the amplitude and duration of each discharge pulse to be digitally monitored. The occasional mea-

surement sequences during which these varied more than 0.5% were discarded.

The decay characteristics of the pulses were found to be even more important than the precise reproducibility of the discharge pulses. Improper matching of the supply to the discharge was found to cause persistent low-level ringing which could then serve to heat the electron gas during the afterglow period. At both pressures in these experiments, matching was sufficient to give less than 100 mV of asynchronous ripple across the electrodes after a period less than the duration of the first interval used in the time-resolved spectroscopic measurements. This was found to be sufficient to ensure there were no spurious heating effects during the afterglow period.

Spectral resolution in the visible region was provided by a 0.75-m tandem Czerny-Turner monochromator with gratings blazed for 5000 Å. A similar instrument with gratings blazed for 3000 Å served in the near ultraviolet. Isolation of the $I_K(2, j)$ atomic lines presented no problem at 1.86 Torr. However, at 44.6 Torr, resolution of the order of 1 Å was required to isolate the atomic lines from the generally more intense molecular bands. Under these conditions, it was found necessary to measure line profiles as functions of time for all $I_K(2, j)$ contributing materially to the absolute intensity sum of Eq. (10). Figure 1 is typical of these and shows the relative profile of the 5015-Å ($3\,^1p \rightarrow 2\,^1S$) transition at five successively larger afterglow times at 44.6 Torr. The limits representing average intensity plus or minus standard deviation are plotted as functions of incremental change in wavelength. The relative similarity of the line shapes is a strong indication that measurements of this line can be considered free of any significant molecular contribution. All other important atomic lines showed similar isolation.

At the higher pressure, an examination of the time dependence of the atomic line intensity following the termination of the ionizing pulse showed all $I_K(2, j)$ to have similar functional dependences, though not the identical similarity found in earlier work at low pressures.[6–9] More detailed observation showed the relative importance of each of the constituents in the intensity sum of Eq. (10) to be continuous, though relatively weak, functions of time and consequently electron density. No single component was found to adequately approximate the functional dependence of the intensity sum for the atomic light on electron density over the range spanned by these measurements, 10^{10}–10^{12} cm^3/sec at 44.6 Torr.

The final determination of the summed intensity was made from absolute intensity measurements of each member of each atomic spectral series, each being individually calibrated against a strip-filament lamp traceable to NBS. Figure 2 shows the resulting total intensities for both pressures. A similar procedure was followed for the intensity of the Saha lines, $I_n(2, Q)$, needed for the application of Eq. (10).

B. Electron Temperatures

Use of the first of the two methods for determining electron temperatures required the accumulation of photon counting rates as functions of wavelength for a constant value of the experimental parameters. This was obtained with the use of a synchronous gate which passed photon counts to

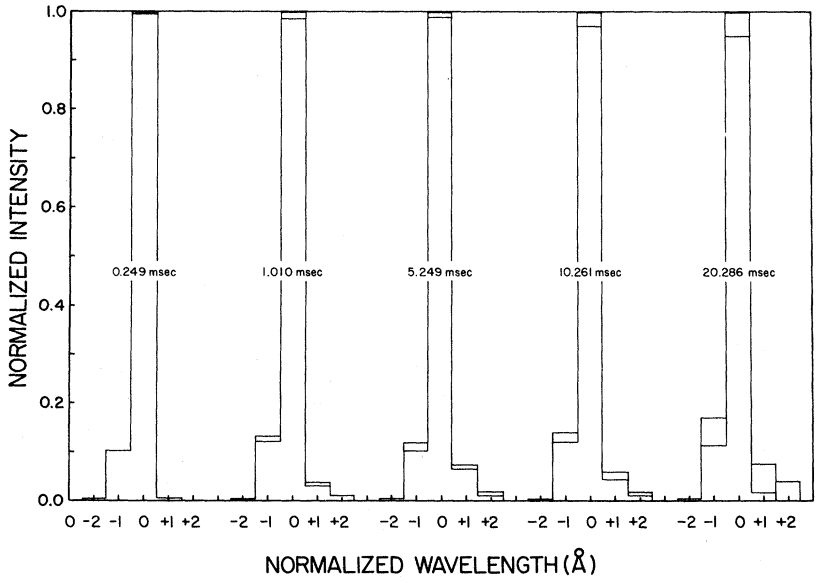

FIG. 1. Graph of normalized intensity as a function of wavelengths of the 5-Å interval centered about 5015 Å. The data are repeated for the five successively later afterglow times indicated. Intensity limits representing data plus or minus one standard deviation of the accumulated data are shown.

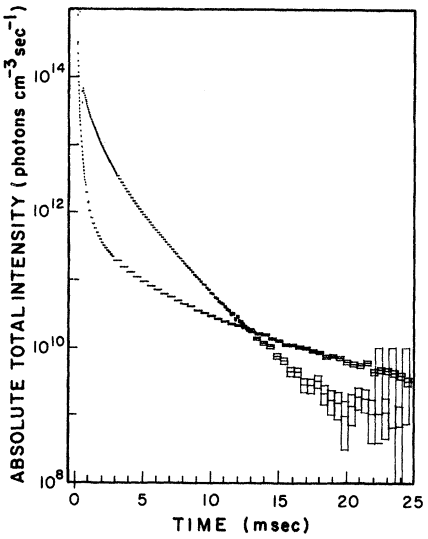

FIG. 2. Graph as a function of time following the initiation of the discharge pulse of the total photon emission rate from atomic helium transitions to levels having $n=2$. The function with the steepest initial slope represents data at a neutral pressure of 44.6 Torr, and the other curve represents data taken at 1.86 Torr. At late times, limits are shown representing the data plus or minus one standard deviation.

the accumulator during a relatively short time interval. This sampling interval occurred at the same delay time into the afterglow period following each successive discharge cycle. The accumulator for this application was a 400-channel multichannel scaler and was connected so that the accumulation address was advanced synchronously with the wavelength drive of the spectrometer. Dispersions of the order of 10 channels/Å were obtained. Usable signals could be collected with a gate duration comparable to the time required for the electron density to decrease by a factor of 2.

The lower curve of Fig. 3(a) shows a typical result for a value of $\Delta U_s < \Delta U_q$ resulting in a well-resolved spectrum of the $n\,^3P \rightarrow 2\,^3S$ series for the earliest afterglow times, 0.025–0.825 msec, as measured from the end of the discharge pulse. As can be seen, discrete lines can be resolved only to a value of q equal to 19 or 20.

As discussed in Sec. II B, greater statistical significance can be obtained by using larger spectrometer slits to integrate the intensity with respect to wavelength. The indicated temperature is unaffected, provided $\Delta U_s \ll KT$. The upper curve in Fig. 3(a) illustrates the improvement obtained and shows the same data as the lower curve, but with ΔU_s for the former significantly greater than for the latter. This figure also suggests a severe practical difficulty, namely, the failure of the free-bound continuum to decrease with wavelength to a value characteristic of the "dark current" from the photomultiplier. This indication is confirmed in Fig. 3(b) which concentrates on the high-energy tail of the continuum corresponding to the same $^3P \rightarrow 2\,^3S$ series. Apparently, a broad-band spurious continuum underlies the desired spectral

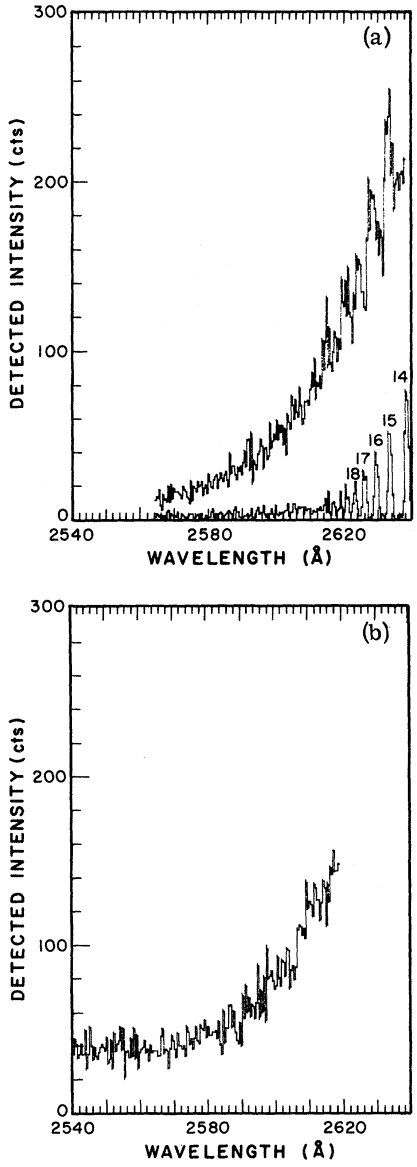

FIG. 3. Graphs of the intensities as functions of wavelength in the spectral region continuing the ionization limit of the $n\,^3P \rightarrow 2\,^3S$ series. (a) Data are presented in terms of the total photon counts recorded during 300 repetitions of the period extending from 0.025 to 0.825 msec from the end of the discharge pulse. Lower curve: $\Delta U_s = 0.07KT$; upper curve: $\Delta U_s = 0.35KT$. (b) Total counts recorded for the period extending from 0.025 to 8.025 msec from the end of the discharge pulse. $\Delta U_s = 0.70KT$.

features. Most probably this can be attributed to the decay of the fluorescence of the quartz window following irradiation by the vacuum ultraviolet emission from the active discharge. In any case, the relative constancy of the intensity with wavelength suggested the procedure of subtracting from the data the background corresponding to the average intensity at the appropriate time measured for the wavelength range lying immediately below the region for which the recombination continuum could be detected.

Additional support for the procedure was provided by the observation that at late afterglow times, the longer-lived spurious continuum showed no wavelength dependence over the range spanned by the data of Figs. 3(a) and 3(b).

Application of the second method for the determination of electron temperature required the measurement of the absolute intensity of a single $I_n(2, q)$, together with the integral over the wavelength of the intensities corresponding to all members of the $^3P \rightarrow 2\,^3S$ series having an upper level with ionization energy greater than U_q. Measurement of this data as a function of time provided the variables needed in Eq. (19) to give the distribution temperature T as a function of time. In practice, a precise knowledge of slit widths and instrument dispersion are necessary and these were calibrated using the scanning techniques of the first method. In addition, it was necessary to subtract the time-resolved record of the spurious continuum from the data. In each measurement, intensities were obtained as photoelectron counting rates with known statistics. Whenever data were combined numerically, the probable errors were combined according to standard statistical techniques. In the case of this second method for electron temperature, the limiting contribution to the total statistical error was from the intensity of the single Saha line, $I_n(2, q)$. These data are shown in Fig. 4, the upper curve of Fig. 4(a) being the counting rate for the $18\,^3P \rightarrow 2\,^3S$ transition at 2624 Å and 1.86-Torr pressure, and Fig. 4(b) being the counting rate for the same transition at 44.6-Torr pressure. The component intensity contributed by the spurious continuum at 1.86 Torr is shown as the lower curve in Fig. 4(a). In each case, the horizontal dimension of the data blocks represents the uncertainty in time caused by the finite duration of each counting interval. Vertically, within each block, the mean counting rate for that time interval and the limits representing that mean rate plus or minus one standard deviation of the counting rate have been indicated.

The counting rates shown in Fig. 4(b), for example, represent the accumulation of 150K afterglow cycles. Since the statistics are essentially Gaussian, a further improvement of only 3 in the signal-to-noise ratio would have necessitated about a 30-h measurement period. Consequently, the data of Fig. 4(b) were considered to be optimized.

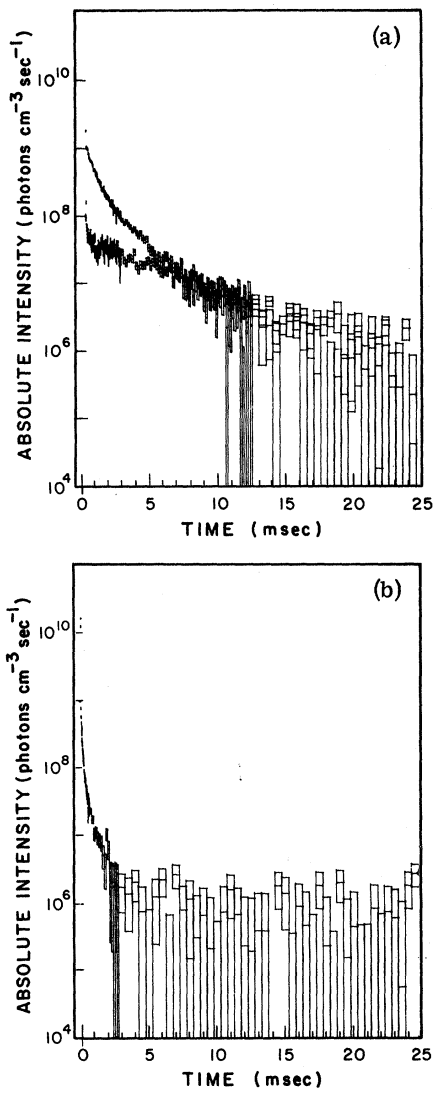

FIG. 4. Graphs as functions of the time following the initiation of the discharge pulse of the photon emission rate from the atomic helium transition $18\,^3P \rightarrow 2\,^3S$ at 2624 Å. Where resolved, limits are shown representing the data ± one standard deviation. (a) Neutral pressure of 1.86 Torr. Upper curve: the absolute intensity of the atomic transition including the spurious continuum; lower curve: the absolute intensity of the spurious continuum. (b) Neutral pressure of 44.6 Torr.

Since these data ultimately appear in the denominator of Eq. (19) for the electron temperature, the late-time excursions to low values cause extreme scatter of the resulting temperature. However, as will be seen, such scattered blocks are easily identified as being nonindicative by their relatively large size, provided standard deviations

are combined as discussed above.

In practice, in these experiments at these low electron temperatures only the relative temperature as a function of time could be inferred from the second method. Equation (19) could not be applied absolutely because of the difficulty of being certain that $\Delta U_s = \Delta U_q$, and therefore that $I_n(2, q)$ had been precisely measured. In the case of the low-pressure data, the first method served to locate the time at which thermalization occurred. Then the relative temperatures of the second method were scaled accordingly. In the case of the high-pressure data, the relative temperature decreased so rapidly to a subsequently constant value that this latter was inferred to be 300 °K. Detailed results are found in Sec. IV A.

C. Electron Densities

To change the parametrization of the measurements from time to electron density, an independent time-resolved measurement of electron density was needed. As discussed above, the optimum technique was found to be one involving use of the 36-GHz Fabry-Perot resonator shown in Fig. 5. The quartz afterglow cell was contained in the device with an orientation placing the windows perpendicular to the axis of Fabry-Perot. The transverse electrodes were sufficiently separated as to lie outside the principal path of propagation. The considerable thickness of the windows caused extensive perturbation of most of the resonances, the type and degree of which depended upon the position of the cell in the resonator. However, as shown in Fig. 6 certain resonances contradicted this behavior, remaining insensitive to the cell position. As could be expected, those resonances correspond approximately to the frequencies for which the quartz windows appear to the microwaves as thick antireflection coatings on the ends of the contained afterglow. A more sophisticated analysis appears in a study of this device[16] and confirms the practice of identifying a usable resonance as being the one least sensitive to the position of the cell.

Once the optimum resonance was found, the Fabry-Perot resonator was tuned to maximize that resonance and a calibration was performed with a gas of known dielectric coefficient. Figure 7 shows the value of Δn_a inferred from Eq. (21) as a function of varying pressure of CO_2 in a cell identical to that containing the afterglow. Data points give measurements of different days and different turning conditions for the same resonance, and the dashed line traces the accepted value. Values inferred for the dielectric coefficient appear to be accurate to parts in 10^6, but of greater importance is that the values of Δn_a approximate the absolute changes in coefficient to within 5%. Linarity is much greater than this figure and was not estimated. Consequently, it is indicated that absolute measurements of the electron density should be accurate to within 5%, which implies the limiting inaccuracies will result from sources other than the Fabry-Perot resonator.

In actual operation with the afterglow, the optimum resonance was found to occur at 31.52556 GHz which corresponded to a mode number of $m = 51$. Such a precise definition of frequency required use of a backward wave oscillator (BWO) phase locked to a crystal harmonic. With this arrangement, less than 1 KHz of residual frequency modulation remained on the microwave signal used to probe the resonator. By controlling the relative

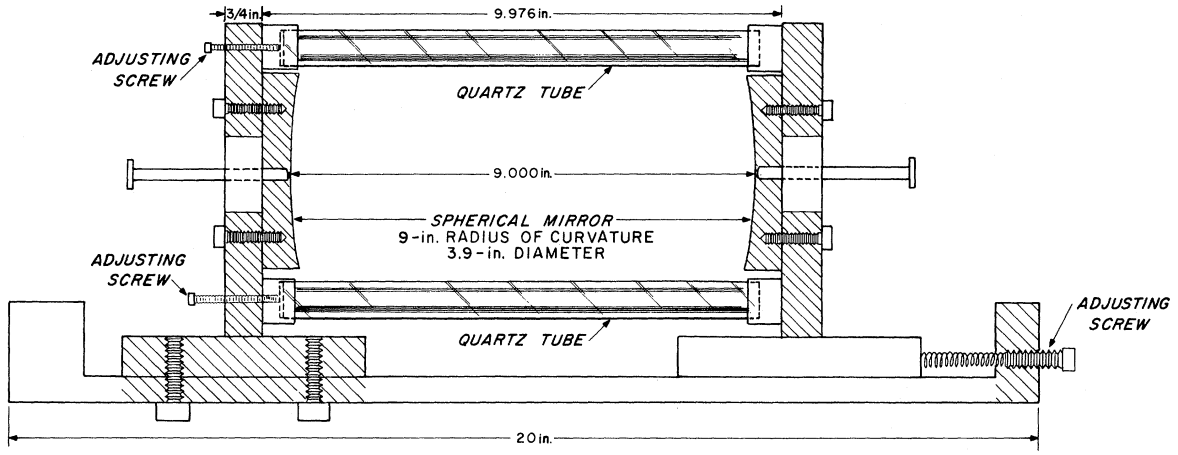

FABRY-PEROT MICROWAVE RESONATOR

FIG. 5. The 36-GHz Fabry-Perot resonator used for electron density measurements.

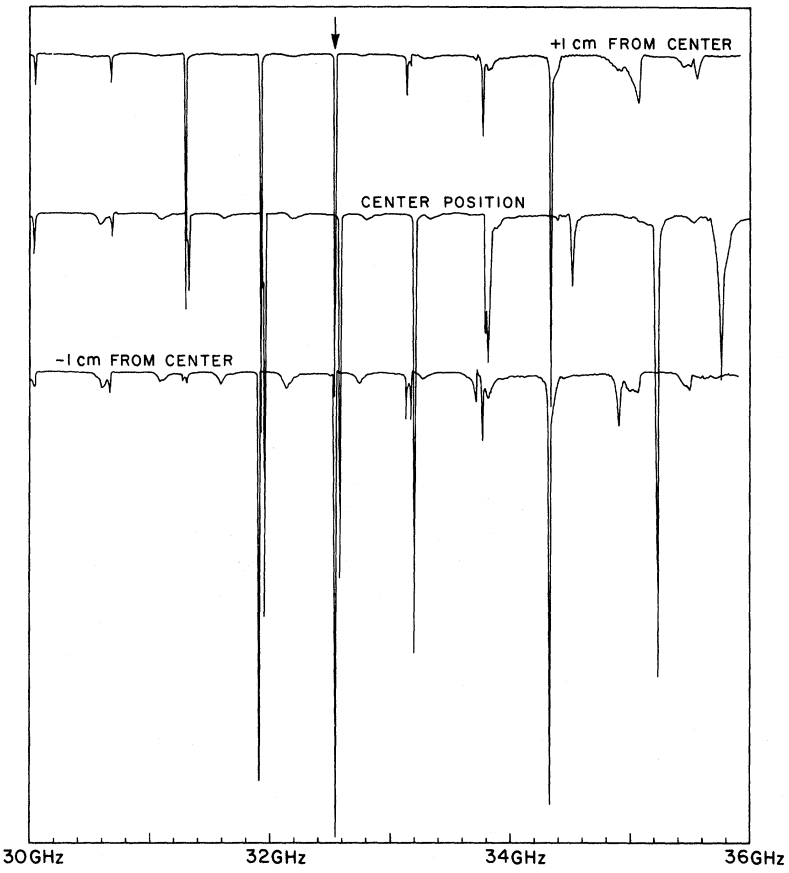

FIG. 6. Graph of the resonator transmission characteristics as functions of frequency. The three different curves correspond to three positions of the afterglow cell in the resonator, each differing by a longitudinal displacement of 1 cm.

phase of the BWO, the cavity could be probed at a frequency slightly shifted from the quiescent resonance. Then, during the afterglow period, a sharp increase in transmission of the resonator could be detected at the time the value of the decreasing electron density corresponded to a dielectric coefficient giving a resonance at the shifted frequency. The degree to which the time could be resolved was a function of the cavity Q. However, the ultimate limit on resolution proved not to be the maximum possible Q, but a lower Q to which the cavity was detuned in order that the time constant of the cavity be small in comparison with the equivalent lifetime of the electron density. This latter factor required that Q be limited to a few thousand. The resulting uncertainties in times at which a particular electron density occurred can be seen in the lower curve of Fig. 8 which represents the 1.86-Torr data.

For completeness, the electron density at 44.6 Torr as a function of time has also been shown as the upper curve in Fig. 8. This data predates the development of the Fabry-Perot techniques and is a composite of microwave interferometric and spectral measurements. The early part of the curve represents the part of the microwave measurement which was relatively insensitive to the undisturbed phase difference in the two paths of the interferometer. Although this phase difference was nominally zero, minute physical instabilities of the system prevented a known zero-phase difference from being obtained. However, only the part of the data beyond 3 msec was sensitive to this problem so the data for that period were obtained from measurements of the absolute intensity of the $I_n(2, Q)$ Saha lines and the analogous bands of the He_2 molecule. Using those measurements, both products $[He_2^+][e]$ and $[He^+][e]$ were obtained from Eq. (1) and its analog for the molecule. The square root of the sum was found to approximate the measured electron density over the early period of the data following electron thermalization. With this agreement of techniques at an early time, it was believed justified to use the hybrid of the two to span the full afterglow period.

IV. RESULTS

A. Electron Temperature

As discussed in Sec. III, the electron and distribution temperatures were obtained in two manners. In the first, the logarithm of time-resolved mea-

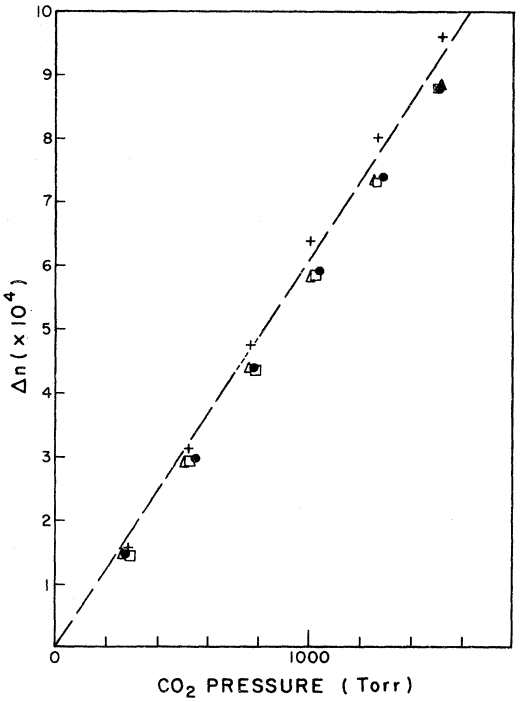

FIG. 7. Calibrating measurement of refractive index change from unity for the indicated pressures of CO_2 in a quartz cell similar to that used in the afterglow measurements. Data points of different shape represent data taken at different times under different alignment conditions. The dashed line plots accepted values from the literature.

surements of the quantity on the left-hand side of Eq. (17) were plotted as functions of ionization energy U. The slope of the resulting curve should then correspond to $(KT)^{-1}$ in the units of U. Figures 9(a) and (b) are typical of these measurements. In Fig. 9(a), the resulting distribution of intensities from the $n\,^3P \rightarrow 2\,^3S$ transitions are shown during the time interval 0.025 to 0.825 msec following the termination of the discharge pulse at 1.86 Torr. Each value of intensity per unit energy interval is shown as a rectangle bounded horizontally by the limits of that interval of energy, $U - \Delta U_s$ and U. The zero of the energy scale has been set arbitrarily equal to the energy of the limit of the $n\,^3P \rightarrow 2\,^3S$ series. The vertical extent of each block corresponds to two standard deviations of the resulting statistical distribution of values on the left-hand side of Eq. (17). The mean value of the statistic is shown as a horizontal line within each block. Where it has been possible to identify a nominal $\Delta U_s \cong \Delta U_q$, the principal quantum number q of the upper state radiating that line has been indicated above the respective block. Radiation from states lying above $19\,^3P$ was not resolved and ΔU_s for values of $U > U_{19}$ were chosen arbitrarily to be of the order of 60 cm^{-1}. A temperature of ~ 380 °K is consistent with these data both for T_e and T.

Figure 9(b) presents the similar results for the distribution of intensities measured during the time interval 2.60 to 4.20 msec following the end of the discharge pulse. A temperature of 300 °K is in agreement with the data.

As discussed previously, better time resolution can be obtained at the expense of counting statistics with the second method which employs Eq. (19). Using the measured counting rates for intensity as functions of time to estimate the left-hand quantity as Eq. (19), and combining the probable errors according to standard statistical techniques, the data of Figs. 10(a) and (b) were obtained.

In both figures, the data have been rescaled to temperatures by requiring $T = 300$ °K at sufficiently late times. In each, the time scale has been adjusted from the scale of Figs. 9(a) and (b) to correspond to the scale of the intensity measurements in which zero occurs at the initiation of the discharge. As in the intensity measurements, the horizontal dimensions of the data blocks indicate the duration of each measurement interval, and the vertical dimension indicates the combined statistical error of the measurements. In addition, in Fig. 9(a) the shaded blocks show temperatures obtained from the first method discussed above. In these blocks, no mean value is shown, as the determination of temperature by that method requires the judgment of a best slope for a curve. The vertical size of the shaded blocks gives a

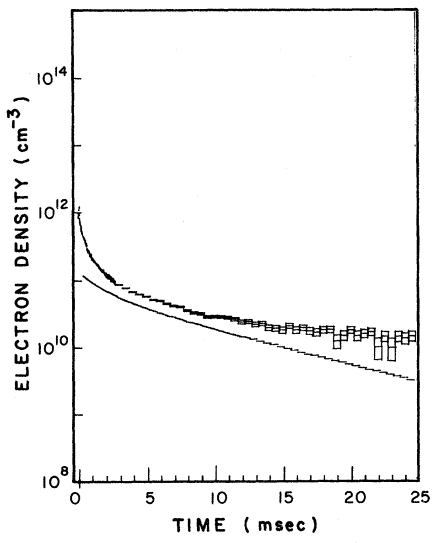

FIG. 8. Electron densities as functions of time following the initiation of the discharge pulse. Upper curve: data for a neutral pressure of 44.6 Torr; lower curve: data for 1.86 Torr.

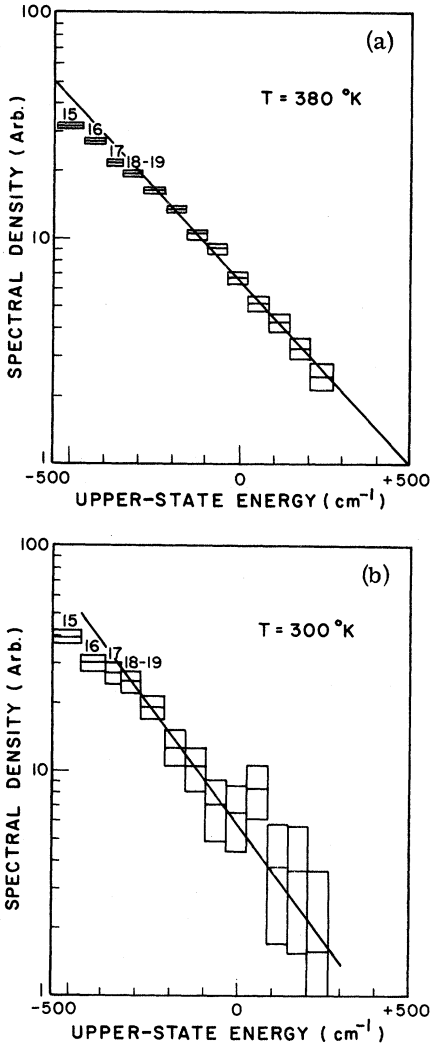

FIG. 9. Measurements at the neutral pressure of 1.86 Torr of the spectral intensities of the $n\,^3P \rightarrow 2\,^3S$ series per unit energy interval of ionization potential of the upper state. Where possible, energy intervals corresponding to discrete transitions have been labeled with the value of n of the upper state. Limits corresponding to the data ± one standard deviation have been shown. The temperatures corresponding to the reciprocal of the slope of the fitted linear approximation are indicated. (a) Measurements taken during the time interval 0.025–0.825 msec following the termination of the discharge pulse. (b) Measurements taken during the time interval 2.6–4.2 msec following the termination of the discharge pulse.

measure of the uncertainty in those judgments.

B. Recombination-Rate Coefficient

To determine the recombination-rate coefficients from Eq. (10), values of T and T_e were needed at afterglow times corresponding to those for which intensity measurements had been obtained. The deterioration of the statistics as a consequence of the repeated combination of measured values necessary to obtain the temperatures of Figs. 10(a) and (b), necessitated the use of longer measurement intervals for the temperatures than for the intensities. In order to apply Eq. (10) to the data available, the temperatures were fit to simple straight-line approximations. The resulting functional representations for 1.86 Torr,

$$T(t) = \begin{cases} 433 - 66.7t & \text{for } t \leq 2 \text{ msec} \\ 300 & \text{for } t > 2 \text{ msec}, \end{cases} \tag{23}$$

and for 44.6 Torr,

$$T(t) = \begin{cases} 465 - 825t & \text{for } t \leq 0.2 \text{ msec} \\ 300 & \text{for } t > 0.2 \text{ msec}, \end{cases} \tag{24}$$

where t is in milliseconds, were subsequently used as sets of statistical variables with errors chosen so that the data blocks for the interpolated values corresponded generally in size to the data blocks of Figs. 10(a) and (b). In practice, this meant that T_e was assumed equal to T with a constant standard deviation of 30 °K.

Combining the temperature and intensity data according to Eq. (10) and plotting the resulting recombination-rate coefficient as a function of the electron density at each of the corresponding afterglow times gives the results shown in Fig. 11. The data points collected at lower electron densities correspond to the 1.86-Torr measurements. Those grouped at the higher electron densities represent the 44.6-Torr results.

It should be reemphasized that the data of this figure comprise a set of independent statistical averages for both ordinates and abscissas over the individual ranges of experimental times shown in Fig. 5. The range of ordinates or abscissas over which the averaging has occurred is indicated qualitatively by the spacing between points and illustrates the need for the large number of measurements which were taken at the consecutively sampled times shown in Figs. 2, 4(a), and 4(b).

C. Temperature Dependence

Though the functional form of the resulting recombination-rate coefficients appears peculiar at first, maxima in such rate coefficients have in fact been predicted theoretically.[20] The return of thermal energy to the electron gas as a result of stabilizing collisions of the type given by (5) has been generally expected to impede the recombination at higher values of electron density. However, the actual thermal economy of a recombining afterglow with a single ion type has been predicted[20] to be quite sensitive to assumptions about the degree of opacity of the plasmas, the values of rate coefficients $K_e(i, j)$ and $K_N(i, j)$, and the lifetimes of the metastable species in the particular after-

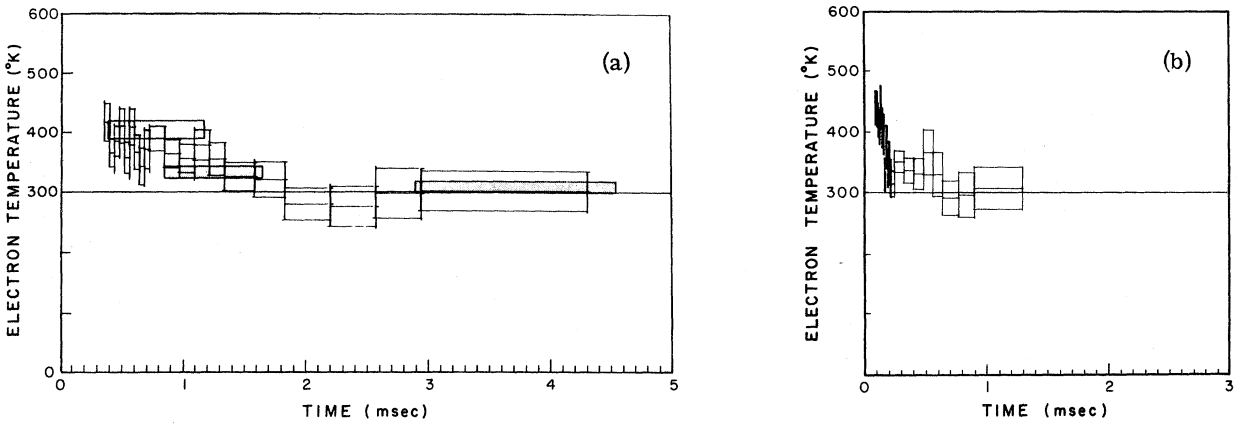

FIG. 10. Electron temperatures as functions of time following the initiation of discharge pulse. (a) Temperatures derived from data taken at 1.86 Torr. Shaded data blocks result from application of Eq. (17), and open data blocks from Eq. (19). In the latter case, the vertical dimensions of each block bound probable errors in temperature and contain the mean value. (b) Temperatures derived from data taken at 44.6 Torr and analyzed according to Eq. (19).

glow considered. Uncertainties in these values coupled with the fact that the thermal economy of the afterglow is affected by the recombination of helium ions other than He^+ makes a comparison of the results presented in Fig. 11 with theory of little significance. Qualitatively, both experiment and theory[20] find maxima in functions representing the dependence of the recombination-rate coefficient on electron density. Both find these maxima between 10^{-9} and 10^{-8} cm^3/sec.

Of considerably greater interest is the comparison of the results of this work with previous measurements made at high electron temperatures (~1000 °K) and densities in the 10^{12}-cm^{-3} region. From this comparison a parametrization of the rate coefficient can be attempted. The observation that the relatively small change in the rate coefficient shown in Fig. 11 resulting from a factor of

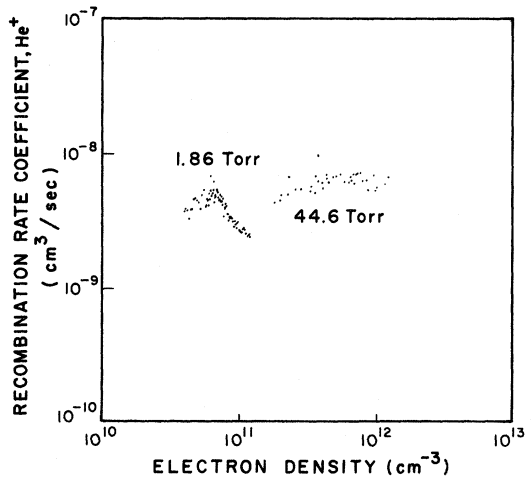

FIG. 11. Graph of the recombination-rate coefficient of He^+ with electrons as a function of electron density. Measurements grouped to lower electron densities result from data taken at 1.86 Torr as marked. Those at higher electron densities result from data taken at 44.6 Torr as marked.

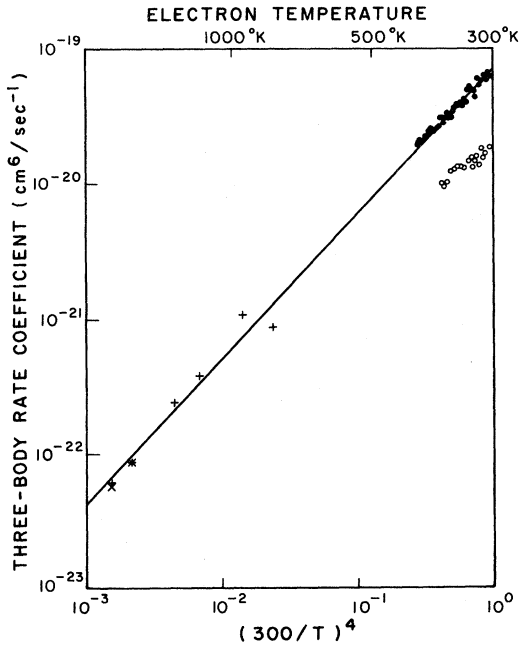

FIG. 12. Logarithmic graph of the recombination-rate coefficient for He^+ expressed as a three-body coefficient and plotted as a function of the logarithm of $(T/300)^{-4}$. Closed circles represent the measurements at 1.86 Torr, open circles the measurements at 44.6 Torr, × the values of Ref. 7, and + the interpretations of Ref. 7 of the work from Ref. 21. The solid line corresponds to Eq. (25).

24 change in pressure suggests that the low-pressure data could be parametrized without the need of a pressure-dependent term. Isothermal theory[1,3,4] suggests a dependence of the rate coefficient on an inverse $\frac{9}{2}$ power of temperature, so the choice was made to plot the logarithm of $\alpha/[e]$ as a function of the logarithm of T^{-4} for convenience. Figure 12 shows the resulting points.

Data from this work appear grouped at the low-temperature upper end of the scale. Points represent the 1.86-Torr data and open circles the 44.6-Torr results. Crosses plot the high-temperature values obtained by Hinnov and Hershberg[7] from measurements of Motley and Kuckes[21] at 0.5 and 4.0 mTorr and ×'s indicate their measurements at 1.2 and 3.8 mTorr.

Quite good agreement is found in Fig. 12 between the 1.86-Torr values of this work, the prior high-temperature work, and the empirical straight line representing the approximation

$$\alpha = 7.1\times10^{-20}[e](T_e/300)^{-4.3}\ \mathrm{cm^3/sec}. \qquad (25)$$

This is to be compared with the value of

$$\alpha_{HH} = 7.8\times10^{-20}[e](T_e/300)^{-4.5}\ \mathrm{cm^3/sec} \qquad (26)$$

calculated by Hinnov and Hershberg from classical considerations. Evidently the mechanism for the stabilization of the recombination of He^+ with electrons is the same at 1.86 Torr and 300 °K as at 0.5 mTorr and temperatures around 1000 °K. It appears that this mechanism is the collisional-radiative process originally suggested by Bates *et al.*[1] in which reaction (5) dominates over reaction (6), as would be expected at these pressures.

The data at the higher pressure, 44.6 Torr, completely contradicts the predictions of later theories[2-4] which include process (6) in the stabilizing sequence. Instead of finding an additive term proportional to pressure of the forms found[11] for the recombination of He_2^+ and predicted by theory,[2] the effect of neutral collisions appears to reduce the recombination-rate coefficient.

It is possible to attribute this effect to the associative ionization of the population of states of sufficiently high ionization potential as to be otherwise stabilized. As a consequence, each $I_K(2, j)$ should contain a term $\{1+R_K(2, j)[\mathrm{He}]\}^{-1}$ relating it to the $I_K(2, j)$ expected in the absence of associative ionization. Then in the zeroth-order approximation, the parametrization of the pressure dependence of α is suggested to be

$$\alpha \propto (1+\gamma P)^{-1}. \qquad (27)$$

Fitting coefficients so that

$$\alpha = 8.1\times10^{-20}[e](1+0.079P)^{-1} \times (T_e/300)^{-4.4}\ \mathrm{cm^3/sec} \qquad (28)$$

is sufficient to produce agreement with the data of Figs. 11 and 12 to within the experimental scatter. Demonstration of the actual utility of Eq. (28) at pressures other than 44.6 Torr for $300 \leq T_e < 400$ °K and values below 1.86 Torr is dependent upon future additional measurements of α at intermediate pressures.

It should be noted that there is some evidence in the distribution of data points corresponding to the higher pressure measurements shown in Fig. 12 that the temperature dependence at 44.6 Torr is weaker than the -4.4 power of Eq. (28). Nevertheless, it appears that over the restricted range covered by that data that the error in using Eq. (28) as an approximation to α is less than the scatter in data.

V. CONCLUSIONS

It is the conclusion of this work that the recombination of He^+ with electrons proceeds principally by the collisional-radiative mechanism as originally proposed.[1] At pressures below 1.86 Torr and temperatures between 300 and 2000 °K the recombination-rate coefficient of He^+ with electrons is reasonably approximated by Eq. (25). The effectiveness of process (6) in stabilizing the recombination of He^+ at higher pressures appears to be more than offset by the destabilizing effect of associative ionization of the excited states. Although the latter can be expected to finally saturate as the pressure is increased because of equilibrium with the inverse process, at pressures not in excess of 44.6 Torr, Eq. (28) is suggested as a reasonable approximation of the recombination-rate coefficient of He^+ with electrons.

The relatively large size of the recombination-rate coefficient, $\sim 10^{-7}$, which would be expected from (26) at electron densities of $1.5\times10^{12}\ \mathrm{cm^{-3}}$ and $T_e = 300$ °K, could make the recombination of He^+ an important loss process for electrons even under conditions for which it was a minority ion. Such a result emphasizes the need to consider individually the components of electron recombination due to each ion type in future experiments.

*Research supported in part by the Atmospheric Sciences Section, National Science Foundation under Grant No. GA-15434, and in part by the National Aeronautics and Space Administration, under Grant No. NGL44-004-001.

†Present address: University College of Wales, Aberystwyth, United Kingdom.

‡Present address: C. E. N. Saclay, B. P. 2, Gif-sur-Yvette, France.

§Present address: Resalab, Box 17040, Dallas, Tex. 75217.

[1] D. R. Bates, A. E. Kingston, and R. W. P. McWhirt-

er, Proc. Roy. Soc. (London) A267, 297 (1962).
[2]D. R. Bates and S. P. Khare, Proc. Phys. Soc. (London) 85, 231 (1965).
[3]R. Deloche, Compt. Rend. 266B, 664 (1968); and R. Deloche and A. Gonfalone, J. Phys. (Paris) 29, 27 (1968).
[4]C. B. Collins, Phys. Rev. 177, 254 (1969).
[5]D. R. Bates, Phys. Rev. 77, 718 (1950); 78, 492 (1950); 82, 103 (1951).
[6]D. E. Kerr, Johns Hopkins University Report, 1960 (unpublished); C. S. Leffel, M. N. Hirsh, and D. E. Kerr (unpublished).
[7]E. Hinnov and J. G. Herschberg, Phys. Rev. 125, 795 (1962).
[8]R. A. Gerber, G. F. Sauter, and H. J. Oskam, Physica 32, 217 (1966).
[9]C. B. Collins and W. B. Hurt, Phys. Rev. 167, 166 (1968).
[10]C. B. Collins, H. S. Hicks, and W. E. Wells, Phys. Rev. A 2, 797 (1970).
[11]J. Berlande, M. Cheret, R. Deloche, A. Gonfalone, and C. Manus, Phys. Rev. A 1, 887 (1970).
[12]A. W. Johnson and J. B. Gerardo, Phys. Rev. Letters, 27, 835 (1971).
[13]C. B. Collins, Phys. Rev. 186, 113 (1969).
[14]M. Gryzinski, Phys. Rev. 115, 374 (1949).
[15]T. Holstein, Phys. Rev. 72, 1212 (1947).
[16]C. B. Collins, B. W. Johnson, H. S. Hicks, and M. J. Shaw (unpublished).
[17]M. A. Heald and C. B. Wharton, *Plasma Diagnostics with Microwaves* (Wiley, New York, 1965), pp. 1–10.
[18]C. B. Collins and W. B. Hurt, Phys. Rev. 177, 257 (1969).
[19]K. B. Persson, J. Appl. Phys. 36, 3086 (1965).
[20]D. R. Bates and A. E. Kingston, Proc. Roy. Soc. (London) A279, 32 (1964).
[21]R. W. Motley and A. F. Kuckes, in *Proceedings of the Fifth International Conference on Ionic Phenomena, Munich*, 1961 (North-Holland, Amsterdam, 1961).

PHYSICAL REVIEW A VOLUME 6, NUMBER 4 OCTOBER 1972

Roton-Limited Mobility of Ions in Superfluid He^4†

Ruben Barrera* and Gordon Baym
Department of Physics, University of Illinois, Urbana, Illinois 61801
(Received 10 April 1972)

We calculate the roton-limited mobility of ions in superfluid He^4 for temperatures below ~1.7 °K. Taking, as a first approximation, a constant ion-roton transition-matrix element, which we treat as an adjustable parameter, we find good agreement with experiment for both positive and negative ions. This model calculation indicates that the most mobile of the recently discovered "exotic" negative carriers is a very light ion.

INTRODUCTION

The mobility of a slowly moving ion in superfluid helium is limited by collisions with the elementary excitations of the liquid. Positive and negative ions have been studied extensively in the last ten years.[1–6] The negative ion is an electron which creates around itself a large spherical bubble of radius ~16 Å at zero pressure; in contrast, a positive ion forms a solid helium sphere of about 6 Å radius, surrounded by high-density liquid (the "snowball" model). Very recently Ihas and Sanders[7] have produced new types of "exotic" negative carriers in superfluid helium, but their structure is still unknown.

At temperatures below ~0.6 °K the mobility of ions is limited mainly by collisions with thermal phonons. At those temperatures mobility measurements have been successfully explained by considering the phonon-ion collision as the scattering of a classical sound wave by an elastic bubble in the case of negative ions,[8] and by a hard sphere in the case of positive ions.[9]

At higher temperatures, above ~0.8 °K, the ionic mobility is limited primarily by collisions of the ions with rotons. In the "kinetic" regime $0.8 \lesssim T \lesssim 1.7$ °K roton-roton scattering can be neglected, while above ~2 °K, roton-roton scattering is so frequent that the rotons appear to the ions as a viscous fluid. Several mobility experiments[10–12] have been performed in the kinetic regime, and they all show a temperature dependence of the mobility μ significantly different for positive and negative ions. The experimental results have been put in the form

$$\mu_{\pm}^{-1} \propto e^{-\Delta_{\pm}/T}, \tag{1}$$

where the subscripts ± refer to positive and negative ions. The values found for Δ_+ are around 8.65–8.8 °K and for Δ_- around 7.7–8.1 °K. Measurements of exotic negative carriers in this temperature region show that the mobility temperature dependence for the "fastest" carrier is of the form (1), but with an exponent $\Delta^* \approx 9.6$ °K. Ihas and Sanders have suggested that this carrier might represent a negative helium ion He^- inside a bubble.

The exponential behavior of (1) is characteristic of the roton-dominated regime and is primarily a reflection of the temperature dependence of the